Sea-State-Dependent Momentum Fluxes for Ocean Modeling

ØYVIND SAETRA AND JON ALBRETSEN

Norwegian Meteorological Institute, Oslo, Norway

PETER A. E. M. JANSSEN

European Centre for Medium-Range Weather Forecasts, Reading, United Kingdom

(Manuscript received 8 March 2006, in final form 29 January 2007)

ABSTRACT

The impact of wave-dependent surface stress on the ocean circulation has been studied using surface stresses calculated from a numerical wave model. The main questions to be investigated were what the effect would be on the Ekman currents in the upper ocean and what the impact would be on storm surge predictions. To answer the first question, the response of wave-dependent forcing on an Ekman type of model was studied. Here, the wave forcing was provided by a one-gridpoint version of the wave model. Second, the impact of the waves was studied with a three-dimensional ocean circulation model for the North Sea. Three different experiments were performed for a period of 1 yr. To test the effect on the storm surge signal, the results have been compared with sea level observations from 22 stations along the Norwegian and Dutch coasts. One of the main findings is that calculating stresses in the wave model, thereby introducing sea-state-dependent momentum fluxes, has a strong positive impact on the storm surge modeling compared with applying a traditional parameterization of surface stresses from the 10-m wind speed. When all cases with sea level deviation from the mean of less than 0.5 m were removed, the root-mean-square error for 1 yr averaged over all stations was reduced by approximately 6 cm. Splitting the momentum budget into an Eulerian and a wave part (Stokes drift) has only a negligible effect on the modeling of the sea surface elevation but increases the angular turning of the Eulerian surface drift to the right of the wind direction with an angle of about 4°.

1. Introduction

In numerical ocean modeling, the momentum fluxes from the atmosphere to the ocean are traditionally calculated from the wind speed provided by an atmospheric model, using a drag coefficient relating the 10-m winds to the surface stress. With this formulation, the surface fluxes are dependent on the local wind speed only. There are at least two problems with this approach. First, unless care is taken that the identical formulation for the momentum flux is used as a boundary condition in both the atmospheric and the ocean models, the net momentum flux is not necessarily conserved. The amount of momentum lost from the atmosphere may be different from the amount of momentum gained by the ocean. A second point is that the surface stress is also, to a large extent, dependent on the sea state, that is, how the wave energy is distributed over the frequency range.

A young wind sea is more dominated by waves in the high-frequency part of the spectrum than an old wind sea, whereas in the latter most of the energy is shifted to the low-frequency part of the spectrum. This has some important implications for the sea surface roughness as experienced by the atmosphere. Short wind waves are rougher than the longer swell and extract momentum more effectively from the atmosphere. Janssen (1991) suggested a theory where the Charnock relation was modified to take the wave age dependence into account. A positive impact of this, on both the results for the atmospheric circulation and the wave field results, was demonstrated by Janssen et al. (2002). Consequently, for operational weather and wave forecasting purposes, the European Centre for Medium-Range Weather Forecasts (ECMWF) has run a coupled wave and atmospheric model system since June 1998.

The effects of sea-state-dependent surface stresses on

Corresponding author address: Øyvind Saetra, Norwegian Meteorological Institute, P.O. Box 43 Blindern, N-0313 Oslo, Norway.
E-mail: oyvind.satra@met.no

DOI: 10.1175/2007JPO3582.1

the storm surge modeling were investigated by Mastenbroek et al. (1993). Using an ocean model coupled to a wave model, they calculated the sea surface elevation for three different storms in the North Sea: 14 February 1989, 27 February 1990, and 13 December 1990. Using time series of observed surface elevation, they compared the results with the model output from a run where the stress was parameterized the traditional way. The results of the coupled wave and storm surge model runs were considerably improved from those based on the stress computed from the 10-m wind speed.

A significant fraction of the momentum lost from the atmosphere is taken up by the wind waves as increased wave momentum. The total wave momentum is the sum of the vertically integrated Stokes drift over all wavelengths. In an Eulerian frame of reference, the wave momentum is only detectable as an average surface drift between the wave trough and the crest. Below the trough, the mean Eulerian wave velocity is zero. Because of both the relatively large time steps used in numerical ocean circulation models and the fact that almost all ocean models impose the hydrostatic approximation, short gravity waves are not present. The bookkeeping of the wave momentum should thus be kept separate from the momentum budget of the ocean model. Only when the waves are dissipated, mostly through wave breaking, does the wave momentum become available for Eulerian mean currents. Accordingly, the appropriate stress to use in an Eulerian ocean model is the fraction of the momentum flux that is not taken up by the waves, plus the momentum lost from the wind-generated waves through dissipation (Weber et al. 2006). By propagation of wave energy, the waves may in this way redistribute the momentum from the atmosphere, both in time and space.

It was demonstrated by Hasselmann (1970) that the Stokes drift yields a force on the mean currents. In a rotating ocean, the along-wave crest velocity component of the wave motion is correlated with the vertical component, inducing a wave stress on the mean Eulerian currents. This stress is proportional to $\mathbf{f} \times \mathbf{U}_s$, where $\mathbf{f}$ is the Coriolis vector and $\mathbf{U}_s$ is the Stokes drift. Following Polton et al. (2005), we will refer to this term as the Coriolis–Stokes forcing. The Coriolis–Stokes term may in some cases be of the same order of magnitude as the wind stress (Xu and Bowen 1994) and is believed by many to be of significant importance for the wind-driven ocean mixed layer (Polton et al. 2005; Jenkins 1989).

Jenkins (1989) revisited the classical Ekman problem (Ekman 1905) by adding the Coriolis–Stokes forcing and wave-dependent stresses. A numerical wave model was used to provide the momentum fluxes and the Stokes drift. Polton et al. (2005) solved a similar problem analytically, using a constant and a linearly varying eddy viscosity. They found that in the Northern Hemisphere the inclusion of the Coriolis–Stokes forcing yields a stronger turning of the Ekman current to the right of the wind direction. Also, by comparing with observations of Ekman currents (Price and Sundermeyer 1999), they found better agreement with the data for the cases when the Coriolis–Stokes forcing was included.

The purpose of this study is to investigate the impact of implementing wave-dependent momentum fluxes in an ocean circulation model by one-way coupling to an ocean wave model. We expect the main impact of this to be on the currents in the wind-driven ocean mixed layer and on the sea surface elevation. Hence, two questions will be addressed: What is the effect of wave-dependent momentum fluxes on the oceanic Ekman layer? And, how will this affect storm surge predictions? To answer the first question, we will start with a detailed study of the upper-ocean response by using a model similar to those used by Jenkins (1989) and Polton et al. (2005). For the turbulent diffusion, a prognostic model for turbulent kinetic energy will used. The surface fluxes of momentum and turbulent kinetic energy will be provided by a one-gridpoint version of the wave model. This means that the Wave Model (WAM; Komen et al. 1994) will be run on one single grid point, disregarding the advection of waves in the horizontal. The advantage of using a simplified model for this part of the investigation is that the surface layer can be far better resolved than what will be possible in a full 3D ocean model.

The next step will be to implement a one-way coupling of the wave model to an ocean circulation model. One reference run (control) and two different experiments will be performed. In the control run, the momentum fluxes will be calculated from the 10-m wind speed using the drag formulation proposed by Large and Pond (1981). In the first experiment, WAM is forced with analyzed winds from ECMWF and provides the momentum fluxes for the ocean model. All the momentum lost from the atmosphere is transferred directly to the ocean surface.

Hence, in this experiment we do not allow the wave model to redistribute momentum in time and space. The only difference between this experiment and the control run is that the magnitude of the surface stress is affected by the wave age. In the second experiment, the momentum flux to the ocean is calculated using the source and sink terms together with the vertically distributed Stokes drift in the wave model.

The structure of this paper is as follows: in section 2,

the equations for the conservation of wave and Eulerian momentum are discussed, and a short description of the numerical models and the observations is given. Section 3 investigates the effects of wave forcing on the mixed layer, using the Ekman model. The results from the full ocean model experiments are then investigated in section 4. A discussion and some concluding remarks are given in section 5.

2. Model and data description

a. Conservation of mass and momentum

Following Janssen et al. (2003), the total wave momentum, **M**, can be expressed in terms of the variance spectrum as

$$\mathbf{M} = \rho g \int d\mathbf{k} \frac{F}{c} \mathbf{1}, \tag{1}$$

where F is the wave spectrum, ρ is the density of water, g is the acceleration of gravity, and c is the phase speed of the gravity waves; $\mathbf{1} = \mathbf{k}/k$ is a unit vector in the direction of the wave propagation, and $\mathbf{k}$ is the wavenumber vector. The equation for conservation of the wave momentum is

$$\frac{\partial \mathbf{M}}{\partial t} + \rho g \boldsymbol{\nabla} \cdot \int d\mathbf{k} \frac{\mathbf{1} c_g}{c} F = \rho g \int \frac{d\mathbf{k}}{c} (S_{\text{in}} + S_{\text{nl}} + S_{\text{diss}} + S_{\text{bot}}) \mathbf{1}, \tag{2}$$

where c_g is the group velocity. The terms in the parentheses are the source terms for input of wave energy, nonlinear wave interaction, dissipation of wave energy, and bottom friction, respectively (Komen et al. 1994).

Let the mean horizontal volume flux per unit area in the ocean be denoted

$$\mathbf{U} = \mathbf{U}_E + \mathbf{U}_S, \tag{3}$$

where $\mathbf{U}_E$ is the Eulerian volume flux and $\mathbf{U}_S$ is the vertically integrated Stokes drift. The conservation of total mass and momentum then yields (Mastenbroek et al. 1993)

$$\left(\frac{\partial}{\partial t} + \mathbf{U} \cdot \boldsymbol{\nabla}_h\right)\mathbf{U} + g\boldsymbol{\nabla}_h \zeta + \frac{1}{\rho}\boldsymbol{\nabla}_h p_a = \mathbf{U} \times \mathbf{f} + \frac{\boldsymbol{\tau}_a - \boldsymbol{\tau}_b}{\rho h} - \frac{1}{\rho h}\boldsymbol{\nabla}_h \cdot \mathbf{S} \tag{4}$$

and

$$\frac{\partial}{\partial t}\zeta + \boldsymbol{\nabla}_h \cdot (h\mathbf{U}) = 0, \tag{5}$$

where h is the depth of the water column, $\boldsymbol{\nabla}_h$ is the horizontal divergence operator, ζ is the sea surface elevation, p_a is the atmospheric pressure, $\boldsymbol{\tau}_a$ is the momentum flux from the atmosphere, and $\boldsymbol{\tau}_b$ represents the bottom stress. The radiation stress tensor **S** is given in terms of the wave energy spectrum by

$$S_{ij} = \rho g \int d\mathbf{k} \left[\frac{c_g}{c} l_i, l_j + \left(\frac{c_g}{c} - \frac{1}{2}\right)\delta_{ij}\right] F(\mathbf{k}). \tag{6}$$

Now, substituting Eq. (2) into Eq. (4) gives the conservation of momentum for the Eulerian ocean currents, $\mathbf{U}_E$, as

$$\left(\frac{\partial}{\partial t} + \mathbf{U}_E \cdot \boldsymbol{\nabla}_h\right)\mathbf{U}_E + g\boldsymbol{\nabla}_h \zeta + \frac{1}{\rho}\boldsymbol{\nabla}_h p_a = \mathbf{U}_S \times \mathbf{f} + \mathbf{U}_E \times \mathbf{f} + \frac{\boldsymbol{\tau}_{\text{oc},a} - \boldsymbol{\tau}_{\text{oc},b}}{\rho h} - \frac{1}{\rho h}\boldsymbol{\nabla}_h \cdot \mathbf{T} \tag{7}$$

and the continuity equation as

$$\frac{\partial}{\partial t}\zeta + \boldsymbol{\nabla}_h \cdot (h\mathbf{U}_E) = -\boldsymbol{\nabla}_h \cdot (h\mathbf{U}_S). \tag{8}$$

Here, **T** is

$$T_{ij} = \rho g \int d\mathbf{k} \left(\frac{c_g}{c} - \frac{1}{2}\right)\delta_{ij} F(\mathbf{k}). \tag{9}$$

The stresses have also been modified accordingly. The surface stress is now

$$\boldsymbol{\tau}_{\text{oc},a} = \boldsymbol{\tau}_a - \rho g \int \frac{d\mathbf{k}}{c} (S_{\text{in}} + S_{\text{nl}} + S_{\text{diss}}), \tag{10}$$

and the bottom stress is

$$\boldsymbol{\tau}_{\text{oc},b} = \boldsymbol{\tau}_b - \rho g \int \frac{d\mathbf{k}}{c} S_{\text{bot}}. \tag{11}$$

b. Numerical ocean model

The ocean model used, an updated version of the sigma-coordinate Princeton Ocean Model (POM; Blumberg and Mellor 1987), is the Norwegian Meteorological Institute's operational version of POM; (MI-POM; Engedahl 1995). The vertically integrated equations (external mode) are separated from the vertical structure equations (internal mode) by mode splitting. This technique permits calculation of a free-surface elevation by solving the velocity transport separately from the three-dimensional velocity and hydrography. The external-mode portion of the model uses a short time step based on the Courant–Friedrichs–Lewy (CFL) condition and the external wave speed, while the internal mode uses a long time step based on the internal wave speed. The vertical mixing coefficients are provided from a second-order-moment turbulence clo-

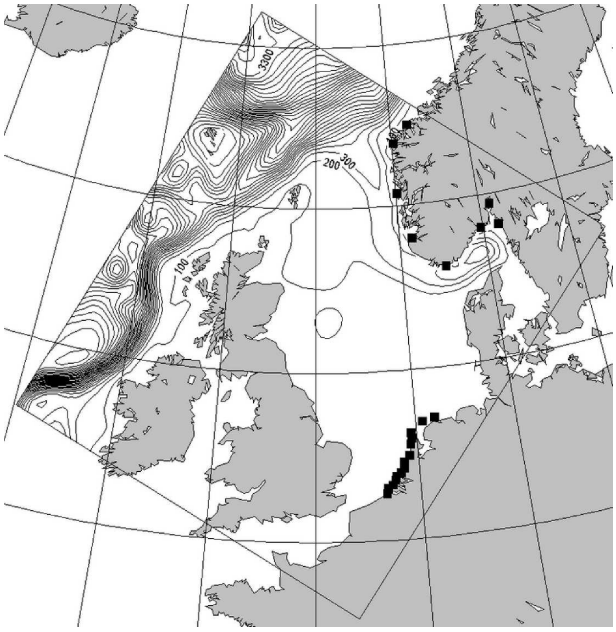

FIG. 1. Model area for the ocean model with 20-km horizontal resolution. Bottom contours are shown every 100 m. The filled squares along the Norwegian and Dutch coasts show the positions of the water level records (listed in Table 1).

TABLE 1. The Norwegian and Dutch water level recording stations used in the model validation.

Station	Lat (°N)	Lon (°E)
Bergen	60.37	05.07
Helgeroa	59.00	09.87
Måløy	61.93	05.12
Oscarsborg	59.68	10.62
Stavanger	58.98	05.73
Tregde	58.00	07.53
Viker	59.03	10.95
Aalesund	62.47	06.15
Brouwershavense Gat	51.75	03.81
Cadzand	51.38	03.38
HA10	51.86	03.86
Den Helder	52.97	04.74
Hoek van Holland	51.97	04.12
Ijmuiden	52.46	04.56
Meetpost	52.27	04.30
Petten	52.79	04.67
Roompot	51.62	03.68
Scheveningen	52.10	04.27
Terschelling	53.44	05.33
Texel	53.12	04.73
Westkapelle	51.52	03.44
Wierumergronden	53.52	05.96

sure submodel (Mellor and Yamada 1982; Galperin et al. 1988).

The grid system is polar stereographic and covers the North Sea and the Skagerrak, and the horizontal grid resolution is 20 km. The model bathymetry derives from an improved version of the 5-minute gridded elevations/bathymetry for the world (ETOPO5) database from the National Geophysical Data Center (Fig. 1).

The model uses 21 sigma levels, with increased resolution in the upper ocean. At the open boundaries, a flow relaxation scheme applies climatological data from the Levitus archive and others (Martinsen et al. 1992), consisting of monthly means of sea surface elevation, currents, salinity, and temperature. The model is also relaxed toward climatological salinity and temperature at depths greater than about 500 m. Fresh and brackish runoff from rivers and/or estuaries were also implemented. Tides are applied to the model by specifying amplitude and phase of sea level and depth-mean currents along the open boundaries. Eight dominant tidal constituents are included: four semidiurnal (M_2, S_2, N_2, and K_2) and four diurnal (K_1, O_1, P_1, and Q_1). The amplitude and phase information for these constituents is obtained from the numerical simulations of Flather (1981) and Gjevik et al. (1994).

The ocean model was initialized using the climatological dataset. The model was spun up 1 yr using analyzed atmospheric variables from ECMWF. The ECMWF data are available every sixth hour with a resolution of approximately 0.5° by 0.5°. We did not apply sea-state-dependent momentum fluxes during the spinup period.

c. Sea level observations

Water level records have been collected from 8 stations along the Norwegian coast (provided by the Norwegian Hydrographic Service) and 14 stations along the Dutch coast (provided by Rijkswaterstaat in Holland), covering 1998. Their names and positions are given in Table 1, and all stations are marked with a filled square in Fig. 1.

Water level is measured every 10th minute at these locations, but only hourly values are used in the model validation. Model values were found by using bilinear interpolation to the location of the station. The water level records typically are located close to the coastline or even deep into fjords. Trying to represent these locations with a coarse model is difficult, and water level fluctuations with shorter periods (as tidal fluctuations) can be misrepresented in the model compared to observations. Since the topic of interest is to examine the representation of atmospheric effects on sea level and not the tide itself, this was compensated by detiding all sea level time series before the validation. A tidal analysis was found for each time series using 59 tidal

constituents. This tidal analysis was then subtracted from the original water level time series. To overcome the problem with reference level for observed and modeled data, the annual mean sea level in each time series was used as a reference level.

3. The Ekman problem with wave forcing

Starting from Eq. (7) for conservation of the Eulerian momentum and neglecting momentum advection, the Ekman problem with wave forcing can be written as

$$\frac{\partial \mathbf{u}}{\partial t} - \mathbf{u} \times \mathbf{f} = \frac{d}{dz}\left(A_w \frac{d\mathbf{u}}{dz}\right) + \mathbf{u}_s \times \mathbf{f}, \tag{12}$$

where $\mathbf{u}$ is the Eulerian velocity vector, $\mathbf{u}_s$ is the Stokes drift vector, and A_w is the eddy viscosity for the vertical diffusion of momentum. From Eq. (10), the boundary condition at the surface is given by

$$-A_w \frac{\partial \mathbf{u}}{\partial z} = \frac{\boldsymbol{\tau}_a}{\rho_w} - g\int \frac{d\mathbf{k}}{c}(S_{\text{in}} + S_{\text{nl}} + S_{\text{diss}}). \tag{13}$$

The minus sign on the left-hand side is because the z axis is taken to be positive downward. In this expression, the momentum lost from the waves is provided to the surface through the boundary condition. This is not necessarily correct. The momentum loss by breaking waves is related to a spontaneous reduction of the Stokes drift. It is therefore reasonable to expect that the momentum loss has a vertical distribution. Jenkins (1989) introduced a general function to express the mechanism for distributing the momentum vertically. For the end results, however, he uses a profile that has the same vertical distribution as the rate of loss of momentum from the Stokes drift. Intuitively, this seems a reasonable choice, which implies that the momentum flux is a source for Eulerian currents at the same vertical level from where it is lost by the waves. By introducing this assumption, the momentum source can be calculated as the negative rate of change of the Stokes drift due to wave breaking. The x and y components of the momentum equation are then written as

$$\frac{\partial u}{\partial t} - fv = \frac{\partial}{\partial z}\left(A_w \frac{\partial u}{\partial z}\right) + fv_s - \left(\frac{\partial u_s}{\partial t}\right)_{\text{diss}} \tag{14}$$

and

$$\frac{\partial v}{\partial t} + fu = \frac{\partial}{\partial z}\left(A_w \frac{\partial v}{\partial z}\right) - fu_s - \left(\frac{\partial v_s}{\partial t}\right)_{\text{diss}}, \tag{15}$$

where u and v are the Eulerian velocity components in the x and y directions, respectively, and u_s and v_s are the velocity components of the Stokes drift. Using the wave spectrum, the Stokes drift is calculated as

$$u_s = 4\pi \int_0^{2\pi}\int_0^{\infty} fke^{-2k|z|}F(f,\theta)\sin(\theta)\,df\,d\theta \tag{16}$$

and

$$v_s = 4\pi \int_0^{2\pi}\int_0^{\infty} fke^{-2k|z|}F(f,\theta)\cos(\theta)\,df\,d\theta. \tag{17}$$

The loss of momentum from the Stokes drift is found by integrating over the dissipation source function in the wave model:

$$\left(\frac{\partial u_s}{\partial t}\right)_{\text{diss}} = 4\pi \int_0^{2\pi}\int_0^{\infty} fke^{-2k|z|}S_{\text{diss}}(f,\theta)\sin(\theta)\,df\,d\theta \tag{18}$$

and

$$\left(\frac{\partial v_s}{\partial t}\right)_{\text{diss}} = 4\pi \int_0^{2\pi}\int_0^{\infty} fke^{-2k|z|}S_{\text{diss}}(f,\theta)\cos(\theta)\,df\,d\theta. \tag{19}$$

When using these expressions, the source function for the dissipation of wave energy must be removed from the boundary condition [Eq. (13)]. The appropriate surface boundary condition for Eqs. (14) and (15) is then

$$-A_w \frac{\partial \mathbf{u}}{\partial z} = \frac{\boldsymbol{\tau}_a}{\rho_w} - g\int \frac{d\mathbf{k}}{c}(S_{\text{in}} + S_{\text{nl}}). \tag{20}$$

At the bottom, a no-slip condition is used:

$$\mathbf{u} = 0. \tag{21}$$

To calculate the turbulent eddy viscosity, we use the $k - \omega$ model proposed by Umlauf et al. (2003). This is a two-equation model for the turbulent kinetic energy, k, and an inverse turbulent time scale, ω. For a nonstratified fluid, the equations are

$$\frac{\partial k}{\partial t} = \frac{\partial}{\partial z}\left(\frac{A_w}{2}\frac{\partial k}{\partial z}\right) + A_w M^2 - (c_\mu^0)^4 k\omega \tag{22}$$

and

$$\frac{\partial \omega}{\partial t} = \frac{\partial}{\partial z}\left(\frac{A_w}{2}\frac{\partial \omega}{\partial z}\right) + c_{\omega 1}M^2 - c_{\omega 2}(c_\mu^0)^4\omega^2. \tag{23}$$

The shear production term, M^2, is given by

$$M^2 = \left(\frac{\partial u}{\partial z}\right)^2 + \left(\frac{\partial v}{\partial z}\right)^2. \tag{24}$$

The empirical constants in the turbulence model are

$$(c_\mu^0, c_{\omega 1}, c_{\omega 2}) = (0.5477, 0.56, 0.83). \tag{25}$$

For more details on the $k - \omega$ model, the reader is referred to Umlauf et al. (2003).

At the surface, the vertical energy flux must be bal-

anced by the release of turbulent kinetic energy from breaking waves,

$$\frac{A_w}{2}\frac{\partial k}{\partial z} = -F_0. \tag{26}$$

Here F_0 is calculated by the wave model as

$$F_0 = \rho g \int_0^{2\pi} \int_0^{\infty} S_{\text{diss}}(f, \theta)\, df\, d\theta. \tag{27}$$

For the lower boundary condition, $z = H$, we assume zero flux of turbulent energy,

$$\frac{\partial k}{\partial z} = 0. \tag{28}$$

The inverse turbulent time scale is related to the mixing length, l, as

$$\omega = \frac{\sqrt{k}}{c_\mu^0\, l}. \tag{29}$$

Near the boundaries, the mixing length is assumed to be a linear function of depth. The boundary conditions for ω are then calculated from the minimum value for the turbulent mixing lengths:

$$l = z_0\kappa, \quad z = 0, \tag{30}$$

and

$$l = z_{0b}\kappa, \quad z = H, \tag{31}$$

where z_0 and z_{0b} are the roughness lengths of the surface and the bottom, respectively, and κ is the von Kármán constant.

According to Terray et al. (1999), the waterside roughness length at the surface is of the order of the wave height. For the experiments in our study, the wave height is about 1 m. Accordingly, this value will be used for all examples in this section.

In this part of the analysis we are mainly interested in the stationary solutions to Eqs. (14), (15), (22), and (23). For numerical reasons, however, the time-dependent problem will be solved by running the model from an initial state with zero velocity until quasi-stationary conditions are obtained. The equations are solved using an implicit numerical scheme. The time derivatives are calculated with first-order forward differences. In the equation for the x direction (14), the velocity u is evaluated at time step $n + 1$. In the equation for the y direction (15), the velocity component v is treated in a similar way. The Coriolis terms are calculated at time step n in both equations.

To provide the external forcing, a one-gridpoint version of WAM has been run for a simulation time of 15 days, using a constant wind speed. This simulation length was chosen to obtain a quasi-stationary sea state. The momentum flux, energy flux, Stokes drift, friction velocity, and significant wave height from the wave model run are then used to force the Ekman model.

Polton et al. (2005) used two sets of observations reported by Price and Sundermeyer (1999) to compare the results for the Ekman current. These are the Long-Term Upper Ocean Study (LOTUS3) and the Eastern Boundary Current (EBC) observations. We will use the same data when comparing with our model results. The LOTUS3 data, used here, are taken over the summer at 35°N in the Sargasso Sea. The average wind stress for this dataset is reported to be 0.07 hPa (hPa = 10^2 Pa). The EBC data are taken at 37°N in the eastern North Pacific during the summer. Here, the average wind stress is 0.09 hPa. It is important to note that in our study, these data have been extracted from the figures in the paper by Price and Sundermeyer (1999). This is of course a rather crude method for obtaining the data and represents a possible source of errors when comparing the model results and the observations.

For each of the two datasets, two experiments and one control run were performed. The control run and experiments were then run with forcing data from both the LOTUS3 and the EBC data. For the LOTUS3 comparison, the surface stress was taken to be 0.07 hPa, and for the EBC comparison, the surface forcing was 0.09 hPa (Price and Sundermeyer 1999). In the control runs, the Stokes–Coriolis term and the term for the dissipation of the Stokes drift in Eqs. (14) and (15) are switched off. In the first experiment, both these terms were reintroduced. Then a second experiment was performed where the dissipation term in the water column due to breaking waves was switched off. The difference between the two experiments was too small to be visible in the plots. Accordingly, only the results from the first experiment, with both effects included, will be shown here.

For the control run then, the appropriate boundary condition is Eq. (13). The results of this are shown as a solid curve in Fig. 2. The dashed lines are the results of the first experiment, and the observations are depicted with a thin solid line with bullets. The figures to the left are from the results when comparing with the EBC data, and the figures to the right are from the results when comparing with the LOTUS3 data. The top panels depict hodograms that display the downwind velocity plotted against the crosswind velocity. The velocities are scaled with the waterside friction velocity, and the depths are scaled with the significant wave height. The middle panel depicts the downwind velocities as func-

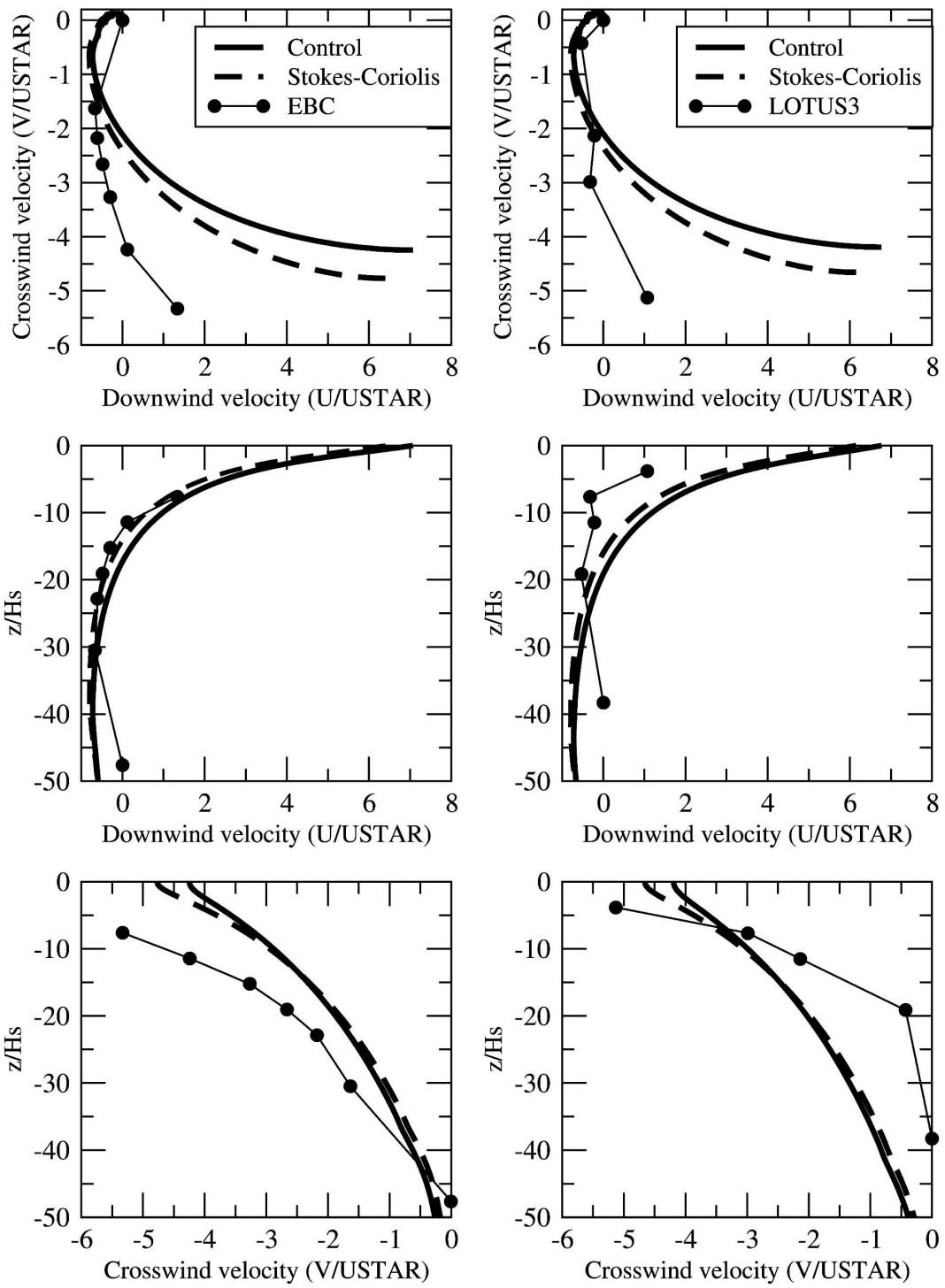

FIG. 2. Results from the runs with and without the Stokes–Coriolis forcing. The dashed lines are with the Stokes–Coriolis term and the solid lines are without this term. The model results are compared with EBC and LOTUS3 data, denoted with filled circles. The (left) EBC and (right) LOTUS3 data. (top) The hodogram where the downwind velocity is plotted against the crosswind velocity. (middle), (bottom) The downwind and crosswind velocities, respectively, as functions of depth. All velocities are scaled with the waterside friction velocity, and depths are scaled with the significant wave height.

tions of depth, and the bottom panel shows the cross-wind velocities.

As mentioned above, we could not see any significant impact of including the momentum lost from breaking waves in the water column through the dissipation terms for the Stokes drift on these experiments. We conclude from this that the momentum flux due to breaking waves is well represented as a surface stress boundary condition.

The most striking impact of introducing the Stokes–Coriolis term is the increased angular turning of the Ekman current. This result is qualitatively in agreement with those reported by Polton et al. (2005). For the control runs, the angular turning of the surface currents was 39.3° for the EBC case and 40.1° for the LOTUS3 case. Introducing the Stokes–Coriolis increases the angular turning to 52.9° and 54.1°, respectively. Accordingly, introducing the Stokes drift in the Coriolis force increased angular turning by about 14° in the two cases discussed here. Both sets of observations show a much larger angular turning than our theoretical results. From the observations, we have no measurements of the surface current. The first observation is at about 5 m in the two datasets. By extrapolating this value to the surface, we obtain an angular turning of about 70°.

4. Ocean model experiments

Now, we present the results from the three full-scale ocean model experiments. Three numerical experiments are run over a simulation period of 1 yr, for 1998. The first experiment is referred to as the control run, where a traditional parameterization of surface stresses from the 10-m wind speed is applied. The momentum flux at the ocean surface is calculated according to Large and Pond (1981) as

$$\tau_x = C_D \rho_a |\mathbf{V}_{10}| U_{10} \quad \text{and} \tag{32}$$

$$\tau_y = C_D \rho_a |\mathbf{V}_{10}| V_{10}, \tag{33}$$

where ρ_a is the air density, and U_{10} and V_{10} are the x and y components of the 10-m wind vector $\mathbf{V}_{10}$. The drag coefficient C_D is linearly dependent on the wind speed for large wind speeds and independent when the wind speed is below the threshold value of 11 m s^{-1}, given as

$$C_D = \begin{cases} 0.0012 & \text{if} \quad |\mathbf{V}_{10}| < 11 \text{ m s}^{-1} \\ (0.49 + 0.065|\mathbf{V}_{10}|)10^{-3} & \text{if} \quad |\mathbf{V}_{10}| \geq 11 \text{ m s}^{-1} \end{cases}. \tag{34}$$

This is a parameterization for the neutral drag coefficient. The near-surface wind profile and buoyant production of turbulent kinetic energy is, in general, dependent on the atmospheric stability. According to Large and Pond (1981), the neutral drag coefficient above is an adequate description over the deep ocean.

Experiment number 1, in which the stresses are calculated in the wave model, introduces sea-state-dependent momentum fluxes. For this experiment, no distinction is made between the Eulerian momentum and the wave momentum. All the momentum lost from the atmosphere is used immediately as forcing for the Eulerian currents.

In the final experiment, experiment number 2, the ocean model is forced with the momentum fluxes available for Eulerian currents. This means that the surface stresses are calculated in the wave model using Eq. (10). For this experiment, the Coriolis–Stokes term, $\mathbf{U}_s \times \mathbf{f}$, has been added to the momentum equation in the model. In addition, the Stokes drift is added to the horizontal divergence term in the continuity equation, Eq. (8). The surface stresses are calculated from Eq. (10); that is, all the momentum flux due to dissipation of gravity waves is introduced at the surface. In the previous section, the effect of providing the momentum flux from breaking waves as a source in the water column was investigated and compared with the results from providing the same amount of momentum as a boundary condition at the surface. We could only detect very small differences in the velocities some few centimeters from the surface. This is taken as evidence that the momentum loss from the waves to Eulerian currents is well represented by a stress term in the surface boundary condition.

The radiation stresses, Eq. (6), and the modified bottom stress, Eq. (11), have not been implemented at the present stage. We assume that this is mainly important in shallow waters. Mastenbroek et al. (1993) implemented the radiation stress in their model and reported that the effect was indeed small. This shortcoming should, however, be taken into consideration when judging the results in our investigation, in particular for the sea level observations in the shallow areas off the Dutch coast.

The depth-dependent Stokes drift can be calculated from the energy spectrum of the gravity waves using Eqs. (16) and (17). This involves integration over frequencies, directions, and a number of vertical levels for all model grid points at every output time step. This is extremely time consuming and slows down the numerical integration of the wave model considerably. To deal with this, some simplifications are introduced.

The volume flux of the Stokes drift is found by integrating Eqs. (16) and (17) in the vertical. The volume transport is mainly confined to the near-surface region,

TABLE 2. Validation statistics for all observations.

	Rms control	Rms expt 1	Rms expt 2	Std dev of obs
Dutch stations	0.117	0.111	0.112	0.203
Norwegian stations	0.068	0.064	0.064	0.025

TABLE 3. Validation statistics for observations with value above 0.5 m.

	Rms control	Rms expt 1	Rms expt 2
Dutch stations	0.235	0.174	0.175
Norwegian stations	0.211	0.157	0.156

and we can safely assume that it vanishes at large depths. The volume fluxes are then expressed as

$$U_s = 2\pi \int_0^{2\pi} \int_0^{\infty} fF(f, \theta) \sin(\theta)\, df\, d\theta \tag{35}$$

and

$$V_s = 2\pi \int_0^{2\pi} \int_0^{\infty} fF(f, \theta) \sin(\theta)\, df\, d\theta. \tag{36}$$

These expressions are calculated in the wave model and transferred to the ocean model. To reproduce a vertical distribution, we assume the Stokes drift represented by one wavelength, in this case the peak wavelength, as

$$u_s = u_0 e^{-2k_p|z|} \tag{37}$$

and

$$v_s = v_0 e^{-2k_p|z|}, \tag{38}$$

where k_p is the peak wavenumber. Integrating Eqs. (37) and (38) in the vertical yields the relationship between the surface drift and the volume transports, Eqs. (35) and (36): $u_0 = 2k_pU_s$ and $v_0 = 2k_pV_s$. Using this method, the total flux due to the Stokes drift will be the same as it would be if Eqs. (16) and (17) were used. But it is important to keep in mind that the vertical distribution of the Stokes drift may be different in the two cases. We tested this by comparing plots of the Stokes drift calculated by the two different methods and found that, in general, using the dominant wave to find the vertical distribution yields a slightly too large drift near the surface and a too weak drift in the deeper layers. Nonetheless, the computer resources needed to calculate the Stokes drift at each grid point would be too demanding at the present stage.

The time series from the control run and the two experiments have been compared with observations from the locations listed in Table 1. The results are summarized in Table 2. To avoid the problem of different reference levels in the observations and the model results, all time series are averaged over the whole year, and the annual mean value is subtracted before the statistics are calculated. This procedure removes any bias in the time series, and, accordingly, no mean errors are presented here. The root-mean-square (rms) errors presented in Table 2 are for the whole of 1998. As a reference value, the standard deviations of the observations are also given. The table gives the mean rms error for the Dutch and the Norwegian stations, respectively. The values are the mean taken over all stations. The rms errors are smaller for the two experiments with wave-dependent surface forcing than for the control run. This is the case for both the Dutch and the Norwegian stations. However, the difference is very small indeed, less than 1 cm. For the Dutch stations the rms errors are approximately half the value of the standard deviation of the observations. For the Norwegian stations, the rms errors are more than twice the value of the standard deviation of the observations.

The storm surge model results are of course mostly of interest when the deviation from the mean sea level is large. When calculating the mean rms-errors from the full time series, the result will be dominated by the cases with very small or no storm surge signal. In Table 3 the data have been stratified, removing all cases when the observed sea level deviation is less than 0.5 m. This gives a rather different picture. For both the Dutch and the Norwegian stations, the mean rms errors for the two experiments with wave-dependent surface forcing are about 6 cm less than for the control runs. The difference between the two experiments, on the other hand, is very small for both datasets. According to these data, introducing sea-state-dependent surface fluxes seems to yield significant positive impact on the sea level prediction. Splitting the momentum budget into an Eulerian and a wave part, however, has little effect on the results for the sea surface elevation.

Figure 3 shows a portion of the time series for two selected Dutch stations, during a storm surge in October 1998. Since the results of the two experiments are similar, only experiment 1 is depicted in this plot. Here, the experiments with wave-age-dependent momentum flux seem to be in better agreement with the observations during the periods when the sea level exceeds 1 m. However, one must keep in mind that this plot only shows a small part of the 1-yr time series.

To demonstrate that wave-dependent momentum fluxes actually improve the simulations of the sea surface elevation, the frequency distributions have been calculated. The results are given in Fig. 4 for the Dutch stations and in Fig. 5 for the Norwegian stations. As

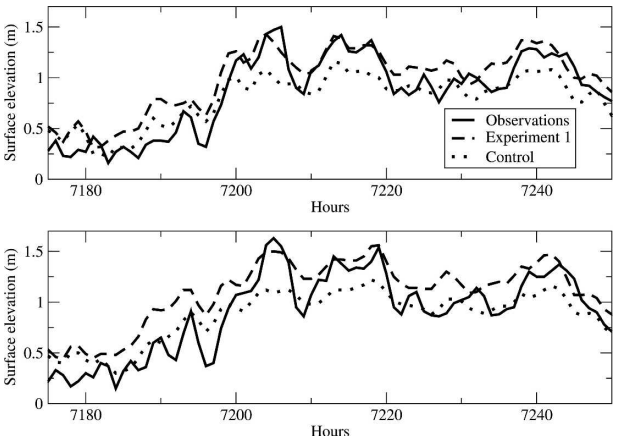

FIG. 3. A portion of the time series of storm surge for two selected Dutch stations (approximately from 27 to 30 Oct 1998).

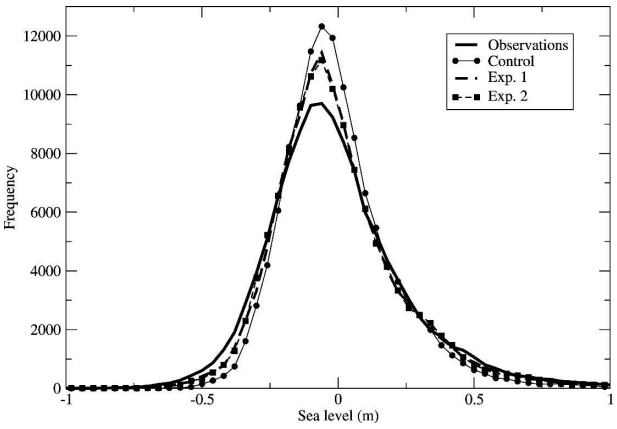

FIG. 4. Frequency distribution of surface elevation for the Dutch coast based on all hourly water level records during 1998 and the corresponding model values.

seen from these plots, the model tends to predict small deviations from the mean sea level too often and large deviations too seldom. This is considerably improved in the simulations where wave-dependent stresses have been used. The impact is most pronounced for the observations from the Dutch stations, where the storm surge signal is stronger. However, the same tendency is also present in the observations from the Norwegian stations. One interesting feature in both figures is that the frequency distribution is not symmetric, implying that the storm surge model is doing better on high sea level than on low. One possible explanation is that because the model imposes a minimum depth at the land boundary, the model does not fully capture the receding sea during the ebb tide. In these experiments the minimum sea depth is 7 m.

Both from the rms statistics and the frequency distributions, it is apparent that the difference between the two experiments with wave-dependent forcing is very small. One conclusion, therefore, is that splitting the momentum budget into an Eulerian and a wave part has only a very small effect on the simulations of sea surface elevation. The results obtained in the previous section indicate that the Stokes–Coriolis forcing would increase the angular turning of the Ekman current. We believe that the reason for the small effect of this on the storm surge signal is that the sea level is mainly determined by the net volume transport in the water column. Even though the surface currents may have a slightly different angular turning in the two experiments, the effect may still be small on the total mass transport.

Based on the results from the previous section, we expect the surface current to have a larger angular turning relative to the wind direction in experiment 2, where the Stokes–Coriolis forcing was introduced. Table 4 shows the mean direction of the surface current averaged over 1 month and over all model grid points. In addition, the mean wind direction is also given. The average is taken over February 1998. The reason for choosing February is that this is the month with the strongest prevailing westerly winds in this dataset. Choosing a period with persistent winds makes it easier to detect an Ekman current in the model data. An example of this is given in Fig. 6, in which the mean currents from experiment 1 are plotted as vectors at various depths. This plot is based on the monthly mean value for February 1998 for an area of 100×100 km^2 outside the Firth of Forth estuary at the Scottish east coast. To see how the currents turn relative to the wind direction, the wind arrow has been plotted as well. At a depth of 50 m, the current is in the opposite direction of the wind, indicating an Ekman depth of approximately this order of magnitude. The angles referred to in Table 4 are relative to the y axis in the model domain, not the geographical north. However, we are only interested in the differences between the various experiments and

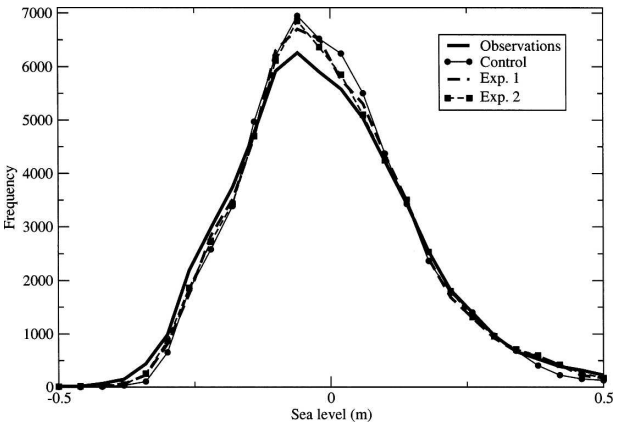

FIG. 5. Same as in Fig. 4, but for the Norwegian coast.

TABLE 4. Monthly mean directions for February. The angles are the average value over all grid points in the model domain, and they are relative to the *y* axis of the model grid (not the geographical north).

	Control	Expt 1	Expt 2	Wind
Angle (°)	149.0	149.5	153.0	130.6

the wind direction, so the absolute direction is not relevant here. For the control run, the mean surface currents are 18.4° to the right of the wind direction. Introducing the wave-age-dependent stresses in experiment 1 increases this angle by 0.5°. For experiment 2 the difference between the mean angles of the control run and the experiment is 4°. Qualitatively, these results are in agreement with those obtained in the previous section. Introducing the Stokes–Coriolis forcing yields an increased turning of the Ekman current. The magnitude of the angular turning, however, is less than what we obtained with the Ekman model. Here, the angular turning of the surface currents in the control run is about 18° to the right of the mean wind direction. In the last experiment, the angular turning was increased by 4°. The equivalent numbers obtained with the Ekman model for this were about 40° and 14°, respectively.

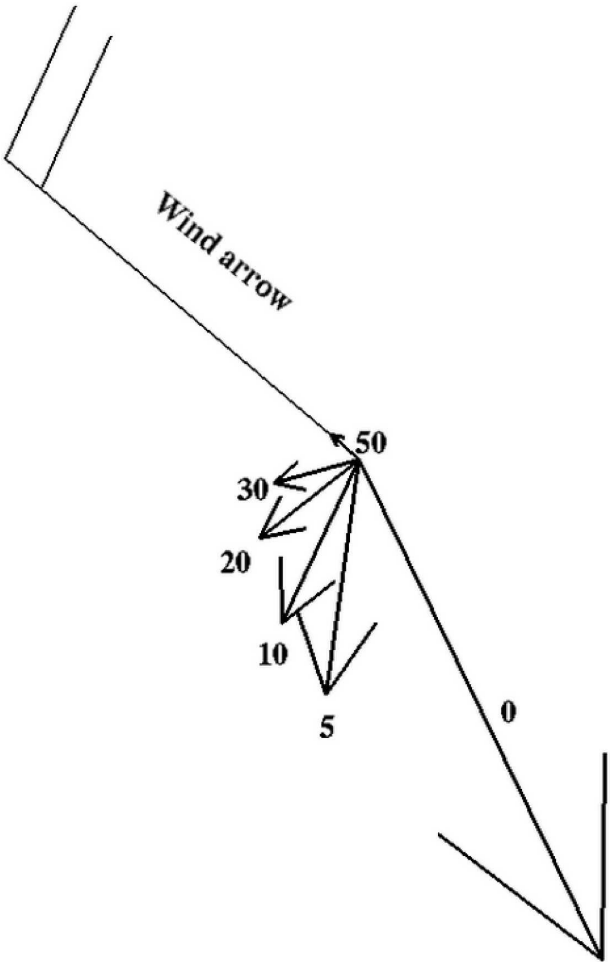

FIG. 6. Mean 10-m wind and currents are shown for expt 1. The average is taken for February 1998 and for an area of about 100 × 100 km^2 outside the Firth of Forth estuary at the Scottish east coast. The mean wind speed is about 9.1 m s^{-1}, denoted by the wind arrow. The mean currents are shown for several depths, denoted by the numbers (m).

5. Conclusions

The impact of wind-generated waves on the ocean circulation has been investigated using a simplified Ekman type of model. Based on the results of this, the effects expected to be most important were implemented into a three-dimensional ocean circulation model, and model simulations for 1 yr were performed. The results were then compared with sea level observations from stations along the Dutch and the Norwegian coast. In agreement with earlier studies, we found that including the Stokes–Coriolis forcing increased the angular turning of the surface currents (Polton et al. 2005). Supplying the momentum flux from breaking waves as a source for Eulerian momentum in the water column, on the other hand, barely affected the currents at all. Accordingly, we believe that the momentum flux from breaking waves is well represented as a boundary condition at the surface. Following the work of Mastenbroek et al. (1993), we also found that the sea-state-dependent stress has a large positive impact on the simulation of storm surges. After removal of tidal influences, the 1-yr simulation with sea-state-dependent stress was in much better agreement with the mean sea level observations from the Dutch and Norwegian coasts than the control simulation, using a traditional formulation for the surface stress. This effect was particularly striking when the dataset was stratified, that is, when all cases with observed sea level deviation from the mean of less than 0.5 m were removed. In this case, the rms error was about 6 cm less for the two experiments than for the control run.

We note that Mastenbroek et al. (1993) considered the evolution of the total current, that is, the sum of the Eulerian part and the wave-induced current. This is an elegant approach, but in such a description there is no Stokes–Coriolis forcing. Why then must we separate the flow into an Eulerian part and a wave-induced part? In the approach by Mastenbroek et al. (1993), momentum is diffused by turbulence to deeper layers, but it is not clear that this also applies to wave momentum. Rather, in the steady state one would expect that wave

momentum is confined to the ocean surface layer, but when the usual turbulence closure is applied to the total current, wave momentum is seen to diffuse to the deeper layers (Janssen et al. 2003). Turbulence closure is normally not applied to the wave-induced part of the current when evolution equations for the Eulerian part of the current are studied, so wave momentum is confined to the surface layer of the ocean.

When the above separation is applied, there is an additional force on the Eulerian part of the current, the Stokes–Coriolis force. Using an operational ocean circulation model for the North Sea and the Norwegian Sea it has been shown that on average this will lead to an additional turning of the Ekman current at the surface of about 4°–5°. This is less than what we obtained with the simplified Ekman model, where an increased angular turning of about 14° was found. Although this had little or no impact on the storm surge signal, an increased angular turning of 4° may be of significant importance for applications that are strongly dependent on the sea surface currents themselves. Examples may, for instance, be simulations of oil drift and trajectory simulations used for search and rescue purposes. We believe that ocean forecasting systems that provide data for such applications would benefit from separating the momentum budget into an Eulerian and a wave-induced part.

Acknowledgments. This research is partly funded by The European Commission through the SEAROUTES project under Contract G3RD-CT-2000-00309 and partly by the Research Council of Norway through the Monitoring the Norwegian Coastal Zone Environment (MONCOZE) project under Contract 143559/431. We thank Jean-Raymond Bildot and Saleh Abdalla for support and valuable discussions. We also thank the Norwegian Hydrographic Service and Rijkswaterstaat in Holland for providing the sea level data.

REFERENCES

Blumberg, A. F., and G. L. Mellor, 1987: A description of a three-dimensional coastal ocean circulation model. *Three-Dimensional Coastal Ocean Models,* N. S. Heaps, Ed., Coastal and Estuarine Sciences Series, Vol. 4, Amer. Geophys. Union, 1–16.

Ekman, V. W., 1905: On the influence of the earth's rotation on ocean currents. *Ark. Mat. Astron. Fys.,* **2,** 1–52.

Engedahl, H., 1995: Implementation of the Princeton ocean model (POM/ECOM-3D) at the Norwegian Meteorological Institute (DNMI). Norwegian Meteorological Institute Research Rep. 5, 40 pp.

Flather, R. A., 1981: Results from a model of the north-east Atlantic relating to the Norwegian coastal current. *Norwegian Coastal Current Symposium,* Vol. 2, R. Stre and M. Mork, Eds., University of Bergen, 31 pp.

Galperin, B., L. H. Kanta, S. Hassid, and A. Rosati, 1988: A quasi-equilibrium turbulent energy model for geophysical flows. *J. Atmos. Sci.,* **45,** 55–62.

Gjevik, B., E. Nøst, and T. Straume, 1994: Model simulations of the tides in the Barents Seas. *J. Geophys. Res.,* **99,** 3337–3350.

Hasselmann, K., 1970: Wave-driven inertial oscillations. *Geophys. Fluid Dyn.,* **1,** 463–502.

Janssen, P. A. E. M., 1991: Quasi-linear theory of wind-wave generation applied to wave forecasting. *J. Phys. Oceanogr.,* **21,** 1631–1642.

——, J. D. Doyle, J. Bidlot, B. Hansen, L. Isaksen, and P. Viterbo, 2002: Impact and feedback of ocean waves on the atmosphere. *Atmosphere–Ocean Interactions,* W. Perrie, Ed., Vol. 1, *Advances in Fluid Mechanics,* WIT Press, 155–197.

——, O. Saetra, C. Wettre, J. Bidlot, and A. Beljaars, 2003: Impact of sea state on atmosphere and ocean. *Proc. ECMWF Workshop on Role of the Upper Ocean in Medium and Extended Range Forecasting,* Reading, United Kingdom, ECMWF, 143–157.

Jenkins, A. D., 1989: The use of a wave prediction model for driving a near-surface current model. *Dtsch. Hydrogr. Z.,* **42,** 134–149.

Komen, G. J., L. Cavaleri, M. Donelan, K. Hasselmann, S. Hasselmann, and P. A. E. M. Janssen, Eds., 1994: *Dynamics and Modelling of Ocean Waves.* Cambridge University Press, 532 pp.

Large, W. G., and S. Pond, 1981: Open ocean momentum flux measurements in moderate to strong winds. *J. Phys. Oceanogr.,* **11,** 324–336.

Martinsen, E. A., H. Engedahl, G. Ottersen, B. Ådlandsvik, H. Loeng, and B. Balino, 1992: MetOcean Modeling Project: Climatological and hydrographical data for hindcast of ocean currents. Norwegian Meteorological Institute Tech. Rep. 100, 93 pp.

Mastenbroek, C., G. J. H. Burgers, and P. A. E. M. Janssen, 1993: The dynamical coupling of a wave model and a storm surge model through the atmospheric boundary layer. *J. Phys. Oceanogr.,* **23,** 1856–1866.

Mellor, G. L., and T. Yamada, 1982: Development of a turbulence closure model for geophysical fluid problems. *Rev. Geophys. Space Phys.,* **20,** 851–875.

Polton, J. E., D. M. Lewis, and S. E. Belcher, 2005: The role of wave-induced Coriolis–Stokes forcing on the wind-driven mixed layer. *J. Phys. Oceanogr.,* **35,** 444–457.

Price, J. F., and A. Sundermeyer, 1999: Stratified Ekman layers. *J. Geophys. Res.,* **104,** 20 467–20 494.

Terray, E. A., W. M. Drennan, and M. A. Donelan, 1999: The vertical structure of shear and dissipation in the ocean surface layer. *Proc. Symp. on the Wind-Driven Air–Sea Interface,* Sydney, Australia, School of Mathematics, University of New South Wales, 239–245.

Umlauf, L., H. Burchard, and K. Hutter, 2003: Extending the $k - \omega$ turbulence model towards oceanic applications. *Ocean Modell.,* **5,** 195–218.

Weber, J. E. H., G. Broström, and Ø. Saetra, 2006: Eulerian versus Lagrangian approaches to the wave-induced transport in the upper ocean. *J. Phys. Oceanogr.,* **36,** 2106–2118.

Xu, Z., and A. J. Bowen, 1994: Wave- and wind-driven flow in water of finite depth. *J. Phys. Oceanogr.,* **24,** 1850–1866.